Magnetic ground states and magnetodielectric effect in $R\mathrm{Cr}(\mathrm{BO_3})_2$ (R = Y and Ho)

R. Sinclair,[1] H. D. Zhou,[1,2] M. Lee,[3,2] E. S. Choi,[2] G. Li,[4] T. Hong,[5] and S. Calder[5]
[1]*Department of Physics and Astronomy, University of Tennessee, Knoxville, Tennessee 37996-1200, USA*
[2]*National High Magnetic Field Laboratory, Florida State University, Tallahassee, Florida 32310, USA*
[3]*Department of Physics, Florida State University, Tallahassee, Florida 32306, USA*
[4]*School of Physics and Materials Science, Anhui University, Hefei, Anhui 230601, People's Republic of China*
[5]*Quantum Condensed Matter Division, Oak Ridge National Laboratory, Oak Ridge, Tennessee 37381, USA*
(Received 7 February 2017; revised manuscript received 4 April 2017; published 8 May 2017)

The layered perovskites $R\mathrm{Cr}(\mathrm{BO_3})_2$ (R = Y and Ho) with magnetic triangular lattices were studied by performing ac/dc susceptibility, specific heat, elastic and inelastic neutron scattering, and dielectric constant measurements. The results show (i) both samples' Cr^{3+} spins order in a canted antiferromagnetic structure with T_N around 8–9 K, while the Ho^{3+} ions do not order down to T = 1.5 K in $\mathrm{HoCr}(\mathrm{BO_3})_2$; (ii) when a critical magnetic field H_C around 2-3 T is applied below T_N, the Cr^{3+} spins in the Y compound and both the Cr^{3+} and Ho^{3+} spins in the Ho compound order in a ferromagnetic state; (iii) both samples exhibit dielectric constant anomalies around the transition temperature and critical field, but the Ho compound displays a much stronger magnetodielectric response. We speculate that this is due to the magnetostriction, which depends on both the Cr^{3+} and the Ho^{3+} ions' ordering in the Ho compound. Moreover, by using linear spin-wave theory to simulate the inelastic neutron scattering data, we estimated the Y compound's intralayer and interlayer exchange strengths as ferromagnetic $J_1 = -0.12$ meV and antiferromagnetic $J_2 = 0.014$ meV, respectively. The competition between different kinds of superexchange interactions results in the ferromagnetic intralayer interaction.

DOI: 10.1103/PhysRevB.95.174410

I. INTRODUCTION

For many years, triangular lattice antiferromagnets (TLAFs) have been studied because of their great potential to exhibit various intriguing magnetic properties related to strong geometrical frustration [1–3]. Recently, studies of TLAFs mainly focus on four central themes: (i) quantum spin liquid (QSL) states [4–8]. For example, this exotic state is realized in $YbMgGaO_4$ [9,10] with an effective spin-1/2 Yb^{3+} triangular lattice in which the spin anisotropy and next-nearest-neighbor interactions play an important role. In another TLAF $Ba_3NiSb_2O_9$ [11,12] with Ni^{2+} (S = 1), the high-pressure modified phase exhibits a QSL state by suppressing the interlayer interactions. (ii) Exotic disordered states [13–17]. One excellent example is the TLAF $NiGa_2S_4$ [18], which exhibits no long-range ordering. Several scenarios, such as nematic or quadrupolar ground states, Kosterlitz-Thouless transitions, and Z_2-vortex transitions, have been proposed for this disordered state [19,20]. (iii) The coplanar 120-deg state and the related field-induced spin-state transitions [21–25]. For instance, $Ba_3CoSb_2O_9$ [26–28], with an equilateral Co^{2+} (effective spin-1/2) triangular lattice, was found to exhibit a 120-deg ordered state at zero field and an up-up-down (uud) phase under a field applied in the ab plane. This unique field-induced state is characterized by a magnetization plateau at a value equal to 1/3 of the saturation magnetization M_s and stabilized by quantum spin fluctuations. (iv) Multiferroicity [29–33]. In several TLAF systems, the ferroelectricity and magnetic ordering are strongly coupled. For example, the TLAF $CuCrO_2$ [34,35] exhibits a spin-driven ferroelectric transition which is dependent upon the system's spiral spin structure. The TLAF $RbFe(MoO_4)_2$ [36–39] shows multiferroic properties in the 120-deg ordered state at zero field, but the ferroelectricity disappears in the field-induced uud phase. The TLAF $Ba_3ANb_2O_9$ (A = Mn) [40] also exhibits multiferroicity exclusively in the 120-deg ordered state, while in the TLAFs $Ba_3ANb_2O_9$ (A = Co and Ni) [41,42], the multiferroicity not only appears at zero field but also survives in the field-induced phases.

Meanwhile, multiferroic properties are also commonly associated with materials with layered structures which can greatly affect their properties, such as magnetoelectric layered perovskites [43–45]. In particular, for layered materials with more than one magnetically active ion, the exchange interactions between the different magnetic ions on different layers possibly induce strong magnetoelectric (ME) behaviors. For example, $SrNdFeO_4$ [46,47] and $NdCrTiO_5$ [48–50] are both layered perovskites with two different active magnetic ions on adjacent layers, and they both exhibit ME behaviors dependent upon the magnetic orderings or spin-flop transitions. The possibility that $NdCrTiO_5$ is multiferroic is still under investigation [51]. Therefore, from a materials engineering perspective, a material with a layered structure, two different magnetic ions, and a magnetic triangular lattice may lead to strong ME or multiferroic properties.

In search of such a material, we chose the system $\mathrm{HoCr}(\mathrm{BO_3})_2$ to investigate. The studies of $\mathrm{HoCr}(\mathrm{BO_3})_2$ have shown that it crystallizes in the rhombohedral space group $R\bar{3}$ and has a dolomite-type structure with a small amount of antisite disorder between the Ho and Cr sites [52]. As shown in Fig. 1(a), both the Ho and Cr ions occupy octahedral sites which form a three-dimensional network by sharing corner-oxygen ions. The BO_3 triangles also share the octahedra's oxygen atoms. Moreover, both the Ho^{3+} and the Cr^{3+} magnetic ions form a triangular lattice in the ab plane, as shown in Fig. 1(b). The intraplanar distance between the Ho/Cr ions is 4.76 Å, and the interplanar distance between the Ho/Cr ions is 5.86 Å. $\mathrm{HoCr}(\mathrm{BO_3})_2$ also shows a magnetic transition at around $T_N \approx 8$ K [52]. Therefore, $\mathrm{HoCr}(\mathrm{BO_3})_2$ meets our requirements listed above for studies on ME behaviors.

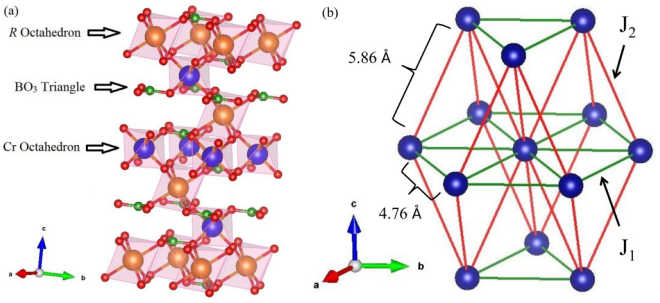

FIG. 1. (a) The dolomite-type crystal structure of $R\mathrm{Cr}(\mathrm{BO}_3)_2$. The orange/blue R/Cr octahedra form a triangular lattice in the ab plane as shown in (b). Only the Cr ions are plotted here. The intralayer and interlayer exchange interactions are labeled as J_1 and J_2, respectively.

So far, no detailed studies on the magnetic and electric properties of this interesting system have been performed. Another advantage here is that we can replace the Ho^{3+} ions with nonmagnetic Y^{3+} ions while retaining the same structure. Thus the comparison between the Y compound with one magnetic ion and the Ho compound with two magnetic ions will help us to better understand how exactly the extra magnetic ion affects the system. With this motivation, we studied the $R\mathrm{Cr}(\mathrm{BO}_3)_2$ (R = Y and Ho) system with various experimental techniques including ac and dc susceptibility, dc magnetization, specific heat, elastic and inelastic neutron scattering, and dielectric constant measurements in order to characterize the magnetic ground states and investigate possible multiferroic properties of the system.

II. EXPERIMENTAL METHODS

Polycrystalline samples of $R\mathrm{Cr}(\mathrm{BO}_3)_2$ (R = Ho and Y) were synthesized by solid-state reactions. The stoichiometric mixture of $\mathrm{Ho}_2\mathrm{O}_3/\mathrm{Y}_2\mathrm{O}_3$, $\mathrm{Cr}_2\mathrm{O}_3$, and $\mathrm{B}_2\mathrm{O}_3$ were ground together and pressed into 6-mm-diam 60-mm rods under 400-atm hydrostatic pressure to form rods of $R\mathrm{Cr}(\mathrm{B}_{1.15}\mathrm{O}_3)_2$ and then calcined in argon at 1100 °C three times: once for 12 h and twice for 36 h each, adding an extra 10% of $\mathrm{Cr}_2\mathrm{O}_3$ by weight before each 36-h annealing.

The zero-field-cooling dc magnetic-susceptibility measurements were performed using a Quantum Design superconducting quantum interference device (SQUID) magnetometer. The ac susceptibility was measured with a homemade setup [53]. The capacitance was measured on thin-plate polycrystalline samples with an Andeen-Hagerling AH-2700A commercial capacitance bridge using a frequency of 20 kHz which was analyzed to obtain the dielectric constant data by approximating the sample as an infinite parallel capacitor. The pyroelectric current was measured using a Keithley 6517A electrometer during warming after the sample was cooled in an electric field from above T_N. The specific heat measurements were performed on a Quantum Design physical property measurement system (PPMS).

Elastic neutron scattering measurements were performed at the Neutron Powder Diffractometer (HB-2A) using a wavelength of either 1.5405 or 2.413 Å to probe the lattice and magnetic Bragg peaks. The powder samples were pressed into rods in order to maintain the powder average in both zero field and applied fields. The inelastic neutron scattering measurements were performed at the Cold Neutron Triple-Axis Spectrometer (CTAX) using a fixed final energy of $E_F = 5.0$ meV in order to investigate a reasonable range of energy transfers and characterize the overall spectrum. Both instruments are located at the High Flux Isotope Reactor (HFIR) at Oak Ridge National Laboratory (ORNL). The neutron scattering diffraction patterns were refined by using the software packages FULLPROF SUITE and SARAH [54,55].

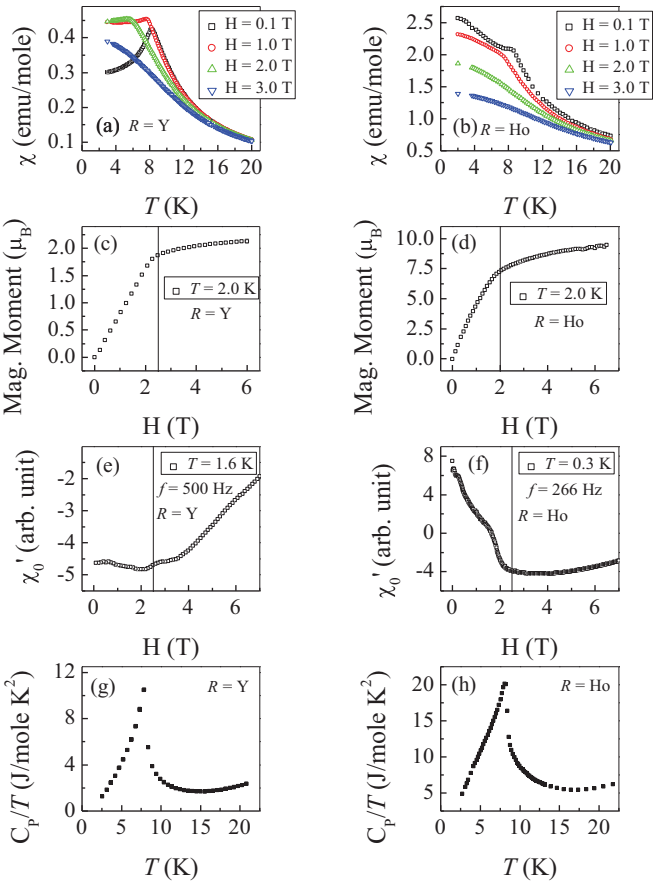

FIG. 2. The temperature dependence of the dc susceptibility for (a) $\mathrm{YCr}(\mathrm{BO}_3)_2$ and (b) $\mathrm{HoCr}(\mathrm{BO}_3)_2$; the magnetization curve for (c) $\mathrm{YCr}(\mathrm{BO}_3)_2$ and (d) $\mathrm{HoCr}(\mathrm{BO}_3)_2$; the field dependence of the ac susceptibility for (e) $\mathrm{YCr}(\mathrm{BO}_3)_2$ and (f) $\mathrm{HoCr}(\mathrm{BO}_3)_2$; the specific heat capacity measured at $H = 0$ T for (g) $\mathrm{YCr}(\mathrm{BO}_3)_2$ and (h) $\mathrm{HoCr}(\mathrm{BO}_3)_2$.

III. EXPERIMENTAL RESULTS

A. ac/dc susceptibility and specific heat

In Fig. 2(a), we show the temperature dependence of the dc magnetic susceptibility measured between $H = 0.1$ and 3.0 T for $\mathrm{YCr}(\mathrm{BO}_3)_2$. At $H = 0.1$ T, there is a sharp peak at $T_N = 8$ K representing a magnetic transition. As the applied field is increased, T_N decreases and the peak begins to broaden. This temperature dependence of T_N suggests that the transition is antiferromagnetic (AFM). At $H = 3.0$ T, T_N is no longer visible down to 2 K. The Curie-Weiss analysis (not shown here) of the $1/\chi$ data above 100 K yields an effective

magnetic moment of $\mu_{\text{eff}} = 3.85\ \mu_B$ and a Curie temperature of $\theta_{\text{CW}} = -1.86$ K, which are in good agreement with the previously reported values [52]. While μ_{eff} matches what one would expect for Cr^{3+} ($S = 3/2$) ions, the dc magnetization measured at 2 K saturates around 2 μ_B, smaller than the expected value of 3 μ_B [Fig. 2(c)]. Currently, it seems that this decreased magnetic moment is likely affected by the R/Cr antisite disorder, which has been characterized by Doi *et al.* [52]. We estimate the antisite disorder in our sample to be ~3% from our elastic neutron scattering Rietveld refinements (as discussed below). There is also a notable slope change in the magnetization data measured at 2 K at around $H = 2.5$ T. Moreover, Fig. 2(e) shows a kink at around $H = 2.5$ T in the ac magnetic-susceptibility data, suggesting a possible phase transition near this critical value, H_C.

Similarly, in Fig. 2(b) the temperature dependence of the dc magnetic susceptibility measured between $H = 0.1$ and 3.0 T for $HoCr(BO_3)_2$ also shows an AFM transition at $T_N = 9$ K which decreases with applied field and vanishes at $H = 3.0$ T. The Curie-Weiss analysis of the $1/\chi$ data above 100 K resulted in an effective magnetic moment of $\mu_{\text{eff}} = 10.99$ μ_B and a Curie temperature of $\theta_{\text{CW}} = -15.1$ K, which are again in good agreement with the previously reported values [52], The dc magnetization measured at 2 K shown in Fig. 2(d) saturates at around 9 μ_B, and there is a slope change which appears around $H = 2.0$ T. The field dependence of the ac susceptibility measured at 0.3 K shown in Fig. 2(f) also reveals a clear feature near $H = 2.0$ T. We again propose that these results indicate a critical field at around $H = 2.0$ T for the system.

The temperature dependence of the zero-field-cooled specific heat measurements is plotted in Figs. 2(g) and 2(h). The data shows sharp λ-type anomalies at the same temperatures that the dc susceptibility measurements showed cusps at $T_N = 8$ K and 9 K for the Y compound and the Ho compound, respectively. This provides further evidence that both materials undergo an AFM transition at these temperatures.

B. Neutron diffraction

Figure 3 shows the neutron powder diffraction (NPD) pattern measured at room temperature for $YCr(BO_3)_2$ and 20 K for $HoCr(BO_3)_2$. Both patterns were measured with a wavelength of 1.5405 Å in order to study the lattice information. The refinements yielded lattice parameters $a =$ 4.764 22(6) Å and $c =$ 15.515 74(28) Å for the Y compound and $a =$ 4.760 02(6) Å and $c =$ 15.492 39(32) Å for the Ho compound. The refinements also show approximately 3% site disorder between the Y/Ho and Cr sites for both samples. Moreover, a small amount of $HoBO_3$ impurity (<5%) was observed in the Ho compound. Both samples were also measured above ($T \approx 20$ K) and below ($T \approx 2$ K) T_N, as well as with applied fields up to $H = 5.0$ T at $T = 1.5$ K using a longer wavelength of 2.413 Å in order to study the magnetic structure information. The samples were prepared as pressed rods to maintain the powder average under applied fields. The diffraction patterns and refinements for the Y compound and the Ho compound can be seen in Figs. 4(a)–4(c) and 6(a)–6(c), respectively.

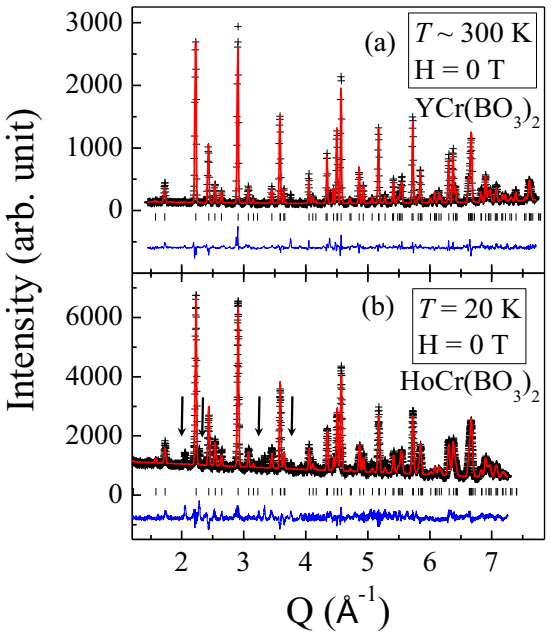

FIG. 3. The elastic neutron diffraction patterns (crosses) for (a) polycrystalline $YCr(BO_3)_2$ at room temperature and zero field and for (b) polycrystalline $HoCr(BO_3)_2$ at $T = 20$ K and zero field using a wavelength of 1.540 5 Å. The solid curves are the best fits from the Rietveld refinements using the FULLPROF SUITE. The vertical marks indicate the position of Bragg reflections, and the bottom curves show the difference between the observed and calculated intensities. The arrows denote $HoBO_3$ impurity peaks.

For $YCr(BO_3)_2$, which contains only a single magnetic ion (Cr^{3+}), the NPD pattern clearly shows extra Bragg peaks at 2 K under zero field [Fig. 4(b)]. These lattice forbidden reflections strongly suggest an AFM spin structure and they can be described by a propagation vector $\mathbf{k} = (0, 0, 3/2)$. The magnetic structure resulting from the diffraction pattern refinement is shown in Fig. 5(c). The Cr^{3+} spins form a ferromagnetic configuration in the ab plane but tilt away from the ab plane with a canting angle of 31.5°. Between the layers, the Cr^{3+} planes align antiferromagnetically.

The intensity of the (0, 0, 3/2) magnetic Bragg reflection was investigated as a function of both temperature and magnetic field, as shown in Figs. 5(a) and 5(b). The reflection not only disappears above T_N but also is suppressed by a critical magnetic field $H_C = 2.5$ T, which agrees with our previous dc and ac susceptibility measurements. The NPD pattern measured at 2 K under $H = 5.0$ T [Fig. 4(c)], larger than H_C, confirms that the material now adopts a ferromagnetic (FM) ground state, which is supported by the observed magnetic Bragg peaks that are at the same positions as the lattice Bragg peaks. This suggests a new propagation vector, $\mathbf{k}_{\text{FM}} = (0\,0\,0)$. As shown in Fig. 5(d), the refinement of the 5.0-T NPD pattern shows that in this FM state, the Cr^{3+} spins are aligned in the ab plane with a canting angle of 40.6° away from the ab plane. Therefore, a magnetic field above H_C flips the AFM arrangements of spins between the layers along the c axis at zero field to ferromagnetic alignments. As shown in Table I, the total magnetic moment for both AFM and FM magnetic ground states is $\mu_{\text{Cr}} \approx 2.5\ \mu_B$, which is close to the

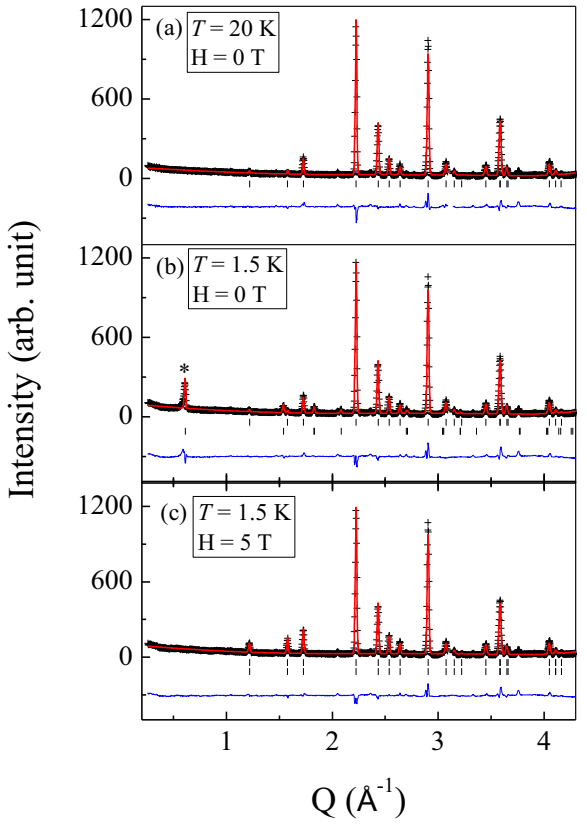

FIG. 4. The neutron diffraction patterns for polycrystalline $YCr(BO_3)_2$ (crosses) at (a) $T = 20$ K and $H = 0$ T, (b) $T = 1.5$ K and $H = 0$ T, and (c) $T = 1.5$ K and $H = 5.0$ T using a neutron wavelength of 2.413 Å. The solid curves are the best fits from the Rietveld refinements using FULLPROF SUITE. The vertical marks indicate the position of Bragg reflections, and the bottom curves show the difference between the observed and calculated intensities. The * in (b) marks the location of the (0, 0, 3/2) reflection.

theoretical value for Cr^{3+} ions as well as the effective magnetic moment derived from our $1/\chi$ data.

While $HoCr(BO_3)_2$ contains two magnetic ions (Cr^{3+}/Ho^{3+}), its magnetic structure at zero field is very similar to that of the Y compounds. Below T_N with no applied field, the system is again described by a propagation vector of $\mathbf{k} = (0, 0, 3/2)$ [Fig. 6(b)]. Analogously to the Y compound, the refinement shows that for $HoCr(BO_3)_2$, the Cr^{3+} spins arrange ferromagnetically with a canting angle of 37.5° away from the ab plane while the Cr^{3+} layers align antiferromagnetically [Fig. 7(c)]. This canting angle is slightly larger than that of the Y compound. Here, no evidence was observed to support the magnetic ordering of the Ho^{3+} spins down to 2 K at zero field. The total refined magnetic moment of $\mu_{Cr} = 3.07(13)\ \mu_B$ as shown in Table II(a) supports this conclusion, as the moment size is close to the theoretical value for Cr^{3+} ions.

Major magnetic Bragg reflections of $HoCr(BO_3)_2$ were also investigated. As shown in Fig. 7(a), the intensities of the (0, 0, 3/2) and the (1, 0, −1/2), (1, −1, 1/2), and (0, 1, 1/2) reflections are suppressed above $T_N = 9$ K. Meanwhile, at 2 K, the intensity of (0, 0, 3/2) is suppressed above $H_C = 2.0$ T, while the intensity of the (1, 0, 1) reflection increases

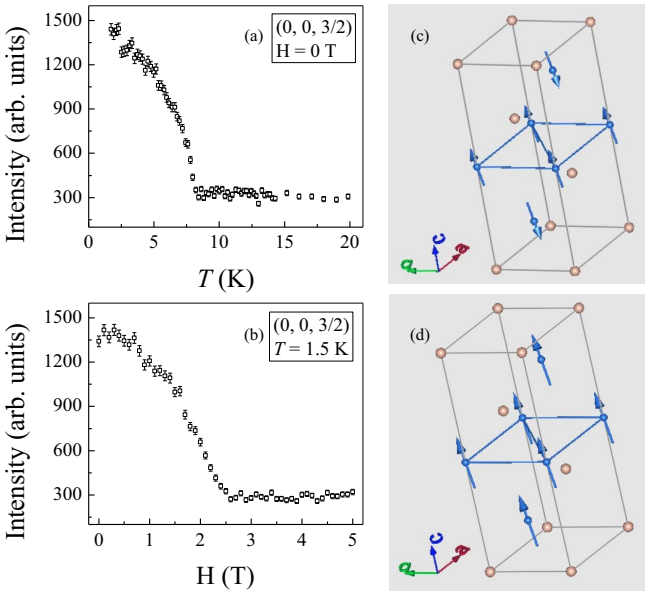

FIG. 5. For $YCr(BO_3)_2$, (a) the temperature dependence and (b) the field dependence of the $(0, 0, 3/2)$ magnetic Bragg reflection, and the magnetic ground state at (c) $H = 0$ T and (d) $H = 5.0$ T.

linearly with increasing field. These critical values agree with our previous susceptibility measurements.

From Fig. 6(c) we can see that the lattice Bragg peaks and magnetic Bragg peaks align exactly for $HoCr(BO_3)_2$ at 2 K and under 4.0 T. This suggests that the system enters a FM ground state above H_C similar to the Y compound. However, the refinement of this data reveals that both the Cr^{3+} and the Ho^{3+} spins order now. The obtained spin structure at 2 K and under 4.0 T is shown in Fig. 7(d), in which both the Ho^{3+} and Cr^{3+} spins are arranged ferromagnetically in the ab plane, but the Cr^{3+} spins have a canting angle of 69.8° away from the ab plane while the Ho^{3+} ions have a canting angle of 80.8° away from the ab plane. The total refined magnetic moment of 10.35(44) μ_B calculated from Table II(b) also supports the fact that now both the Cr^{3+} and the Ho^{3+} spins order and contribute to the value of the magnetic moment. This value also matches closely with the saturation value determined from the magnetization curve as well as the effective magnetic moment derived from our $1/\chi$ data.

By analyzing the magnetic structure information obtained from the neutron diffraction data combined with the previously determined structural information, we were able to obtain two possible magnetic space groups, $R_I\bar{3}$ and $P_S\bar{1}$, using the Bilbao Crystallographic Server [56–59]. While the $P_S\bar{1}$ magnetic space group allows for the magnetic moment to freely align along any direction, $R_I\bar{3}$ completely restricts the magnetic moment to the c axis. Moreover, the Rietveld refinements of the system reveal that the existence of the intense (0, 0, 3/2) peak depends upon having a magnetic moment in the ab plane. Therefore, our data strongly suggests that the system is best described by the $P_S\bar{1}$ magnetic space group.

C. Inelastic neutron

Figure 8 shows the inelastic neutron scattering profiles measured at 20 K and 1.5 K with various momentum transfers

TABLE I. Magnetic moments for $YCr(BO_3)_2$ at $T = 1.5$ K determined from refined neutron diffraction measurements for (a) $H = 0$ T and (b) $H = 5.0$ T.

$YCr(BO_3)_2$	Atom	x	y	z	Mx	My	Mz	M
(a)	Cr1	0	0	0	2.11(17)	2.11(17)	1.29(5)	2.47(24)
$T = 1.5$ K	Cr2	2/3	1/3	1/3	–2.11(17)	–2.11(17)	–1.29(5)	2.47(24)
$H = 0$ T	Cr3	1/3	2/3	2/3	–2.11(17)	–2.11(17)	–1.29(5)	2.47(24)
(b)	Cr1	0	0	0	2.41(17)	2.41(17)	2.06(15)	3.17(28)
$T = 1.5$ K	Cr2	2/3	1/3	1/3	2.41(15)	2.41(15)	2.06(15)	3.17(28)
$H = 5.0$ T	Cr3	1/3	2/3	2/3	2.41(15)	2.41(15)	2.06(15)	3.17(28)

(Q) ranging from 0.5 Å^{-1} to 1.5 Å^{-1}. At each Q, a peak in the intensity with the energy transfer (E) between 1 and 2 meV is clearly observed at 1.5 K which should represent the spin-wave excitation in the magnetic ordered state. This feature disappears in the 20 K data, suggesting that the observed peak is from the magnetic origin.

The spin-wave excitation was analyzed to produce a spin-wave spectrum within a limited E-Q space, as shown in Fig. 9(a). The first branch of the spectrum is visible in our region of interest. The feature flattens out at around $Q = 0.8$ Å^{-1} and peaks near 1.5 meV. From the location of the magnetic peaks in Fig. 4(b), we expect the first zone boundary of the spectrum to be centered near $Q = 0.60$ Å^{-1} and the second zone boundary to be centered near $Q = 1.53$ Å^{-1}.

In order to simulate this spin-wave spectrum, we used the MATLAB library SPINW to model the system [60]. SPINW uses classical Monte Carlo simulations as well as linear spin-wave theory in order to solve the spin Hamiltonian:

$$H = \sum_{i,j} S_i J_{ij} S_j, \tag{1}$$

where S_i are spin vector operators and J_{ij} are 3×3 matrices which describe pair coupling between spins.

For our model, we examined the nearest neighbor (NN) intralayer interaction J_1 as well as the next-nearest neighbor (NNN) interlayer interaction J_2. The values for J_1 and J_2 were determined empirically by comparing the simulated spin-wave spectrum against the experimental data. $J_1 = -0.12$ meV determines the general size and location of the feature, and $J_2 = 0.014$ meV determines the slope of the branch. Specifically, J_2 changed the initial energy value where the

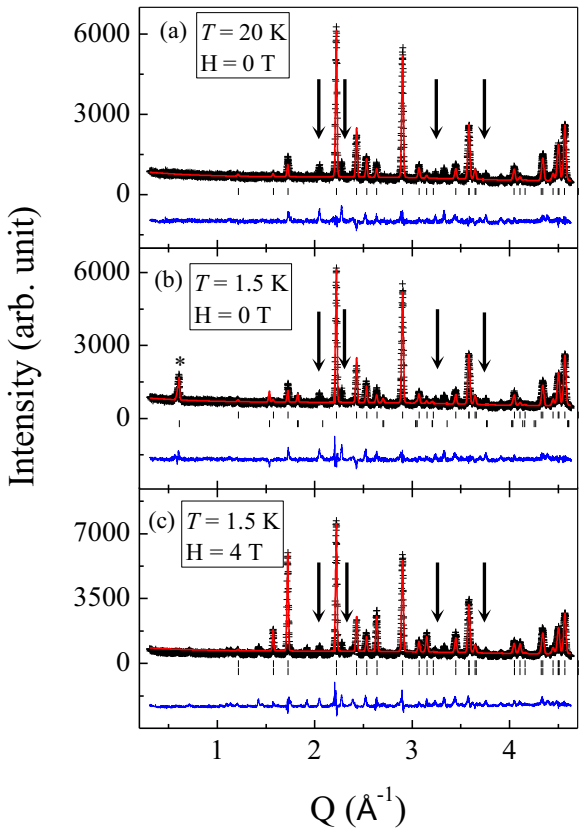

FIG. 6. The neutron diffraction patterns for polycrystalline $HoCr(BO_3)_2$ (crosses) at (a) $T = 20$ K and $H = 0$ T, (b) $T = 1.5$ K and $H = 0$ T, and (c) $T = 1.5$ K and $H = 4.0$ T using a neutron wavelength of 2.413 Å. The solid curves are the best fits from the Rietveld refinements using the FULLPROF SUITE. The vertical marks indicate the position of Bragg reflections, and the bottom curves show the difference between the observed and calculated intensities. The * in (b) marks the location of the (0, 0, 3/2) reflection. The arrows denote $HoBO_3$ impurity peaks.

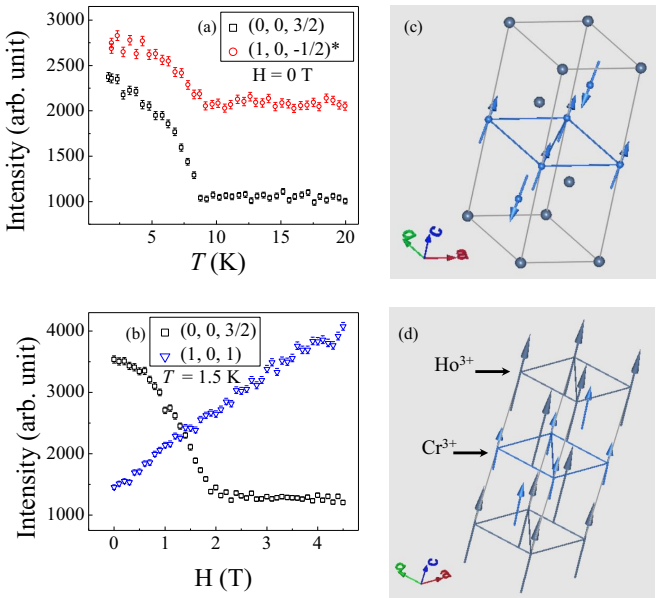

FIG. 7. For $HoCr(BO_3)_2$, (a) the temperature dependence and (b) the field dependence of certain magnetic and lattice Bragg reflections, and the magnetic ground state at (c) $H = 0$ T and (d) $H = 4.0$ T. *Note that the reflection marked (1, 0, −1/2) in (a) also includes intensity from the (1, −1, 1/2) and (0, 1, 1/2) reflections.

TABLE II. Magnetic moments for $HoCr(BO_3)_2$ at $T = 1.5$ K determined from refined neutron diffraction measurements for (a) $H = 0$ T and (b) $H = 4.0$ T.

$HoCr(BO_3)_2$	Atom	x	y	z	Mx	My	Mz	M
(a)	Cr1	0	0	0	2.44(9)	2.44(9)	1.87(4)	3.07(13)
	Cr2	2/3	1/3	1/3	−2.44(9)	−2.44(9)	−1.87(4)	3.07(13)
$T = 1.5$ K	Cr3	1/3	2/3	2/3	−2.44(9)	−2.44(9)	−1.87(4)	3.07(13)
$H = 0$ T	Ho1	0	0	1/2	0.0	0.0	0.0	0.0
	Ho2	2/3	1/3	5/6	0.0	0.0	0.0	0.0
	Ho3	1/3	2/3	1/6	0.0	0.0	0.0	0.0
(b)	Cr1	0	0	0	1.19(11)	1.19(11)	3.25(31)	3.46(35)
	Cr2	2/3	1/3	1/3	1.19(11)	1.19(11)	3.25(31)	3.46(35)
$T = 1.5$ K	Cr3	1/3	2/3	2/3	1.19(11)	1.19(11)	3.25(31)	3.46(35)
$H = 4.0$T	Ho1	0	0	1/2	1.10(8)	1.10(8)	6.80(25)	6.89(27)
	Ho2	2/3	1/3	5/6	1.10(8)	1.10(8)	6.80(25)	6.89(27)
	Ho3	1/3	2/3	1/6	1.10(8)	1.10(8)	6.80(25)	6.89(27)

branch begins at $Q = 0.50$ Å^{-1} and the maximum energy value of the branch achieved near $Q = 0.90$ Å^{-1}. Several values of J_1 and J_2 were tested in order to closely match the experimental results.

The final result is shown in Fig. 9(b). The simulation was constructed using a finite energy resolution consistent with the elastic line for $E_F = 5.0$ meV of $dE = 0.3$ meV. Similar to the measured data, the simulation shows one branch which begins near 1.0–1.2 meV at $Q = 0.50$ Å^{-1}, flattens around $Q = 0.80$ Å^{-1}, and fades into the second zone boundary. Moreover, both the measured and the calculated data show very little intensity below 1.0 meV of transferred energy. Although we expected to find a spin gap with a magnitude close to 0.5 meV, both the measured data and the simulation appear to be gapless. Our simulation provides a good overall agreement with the experimental data, which reasonably suggests that the intralayer interaction is about 1 order of magnitude stronger than the interlayer interaction in $YCr(BO_3)_2$.

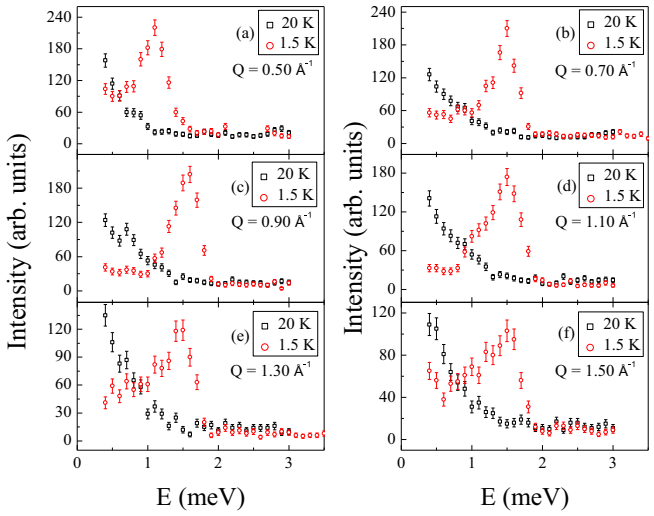

FIG. 8. Inelastic neutron scattering profile above (black squares) and below (red circles) the transition temperature with $E_F = 5.0$ meV centered at (a) $Q = 0.50$ Å^{-1}, (b) $Q = 0.70$ Å^{-1}, (c) $Q = 0.90$ Å^{-1}, (d) $Q = 1.10$ Å^{-1}, (e) $Q = 1.30$ Å^{-1}, and (f) $Q = 1.50$ Å^{-1}. Note that a spurion centered at around 2.3 meV has been removed from (a).

D. Dielectric constant

Figure 10(a) shows the temperature dependence of the dielectric constant ε for $YCr(BO_3)_2$. At zero field, ε shows a cusp near 8 K. While this feature broadens consistently with the strength of the applied field, the amplitude and transition temperature are more complicated. The amplitude increases with increasing applied field up to the critical field $H = 3.0$ T, at which point it begins to decrease as the applied fields get even larger. On the other hand, the transition temperature decreases with increasing applied field up to $H = 3.0$ T and then increases with larger applied fields. The temperature dependence of ε for $HoCr(BO_3)_2$ exhibits a more drastic response. In Fig. 10(b), a broad feature around $T = 4$ K is observed at zero field. As the field increases, this shoulder feature becomes suppressed and vanishes near $H = 1.0$ T. Meanwhile, a sharp peak appears near $T = 7$ K, which increases in relation to the field up to $H = 1.0$ T, at which point it begins to weaken with increasing field. Furthermore, the critical temperature associated with the sharp peak decreases with increasing field.

Figure 11(a) shows the magnetic field dependence of ε for $YCr(BO_3)_2$. Below $T = 1.5$ K, the data shows a sharp peak at around $H = 3.0$ T, as well as a clear minimum near $H = 1.5$ T. Above $T = 1.5$ K, only the sharp peak near $H = 3.0$ T remains visible. Above T_N, this behavior disappears. The magnetic field dependence of ε for $HoCr(BO_3)_2$ is presented in Fig. 11(b). At temperatures lower than its T_N, ε increases sharply at low fields and then saturates into a broad feature at around $H = 1.5$ T. Similar to the Y compound, above its transition temperature, such behavior disappears.

These anomalies, observed from ε for both the Ho compound and the Y compound, are all observed around their magnetic ordering temperatures or critical fields for spin-state transitions; therefore, both systems exhibit some degree of magnetodielectric (MD) coupling. Furthermore, the replacement of the nonmagnetic Y^{3+} ion with the magnetic Ho^{3+} ion affects this coupling, which leads to stronger MD phenomena as revealed by the sharp peak around T_N in the

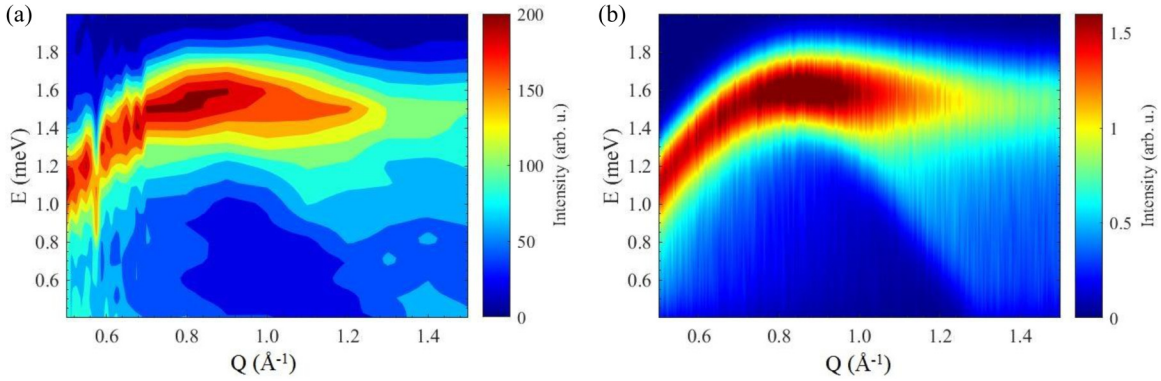

FIG. 9. The (a) measured and (b) calculated powder-averaged spin-wave dispersion for $YCr(BO_3)_2$ measured at $T = 1.5$ K.

field-induced ε data. It is also worth noting that the Ho compound shows little response at zero field near T_N, in stark contrast to the Y compound. Thus the MD phenomena are likely related to different mechanisms for each sample, such as spin-phonon coupling or magnetostriction.

While both compounds were studied via pyroelectric current measurements at different magnetic fields, no electric polarization was observed for either bulk polycrystalline sample around the transition temperatures. It is possible that a single-crystal sample could produce an anisotropic polarization which is hidden by the powder averaging of the results or that the system is already ordered in an antiferroelectric state. Further experiments, including polarization vs electric field hysteresis measurements on single-crystal samples, may be necessary to elucidate the matter.

IV. DISCUSSION

The two compounds share several characteristics of their magnetic properties. The Cr^{3+} spins of both samples enter

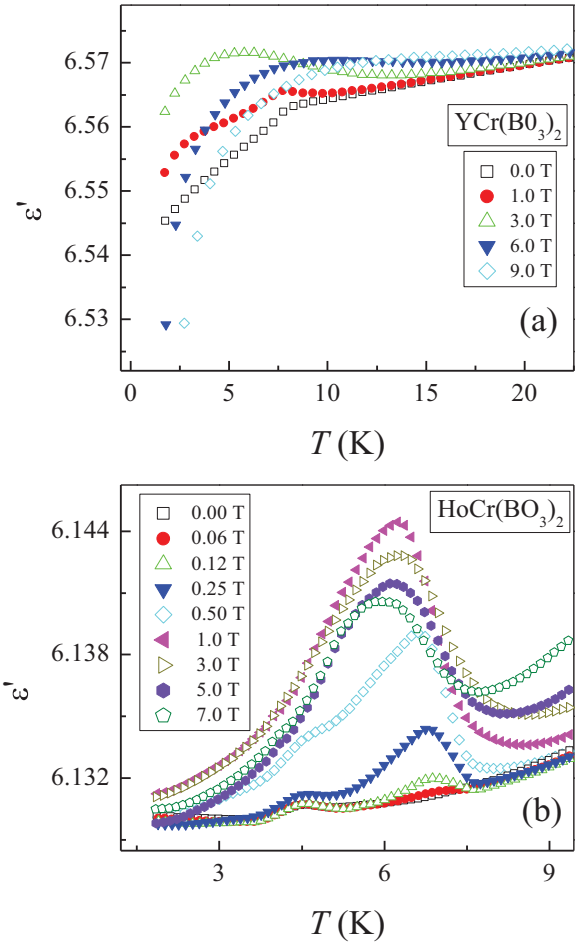

FIG. 10. The temperature dependence of the dielectric constant measured at 20 kHz under applied fields for (a) $YCr(BO_3)_2$ and (b) $HoCr(BO_3)_2$.

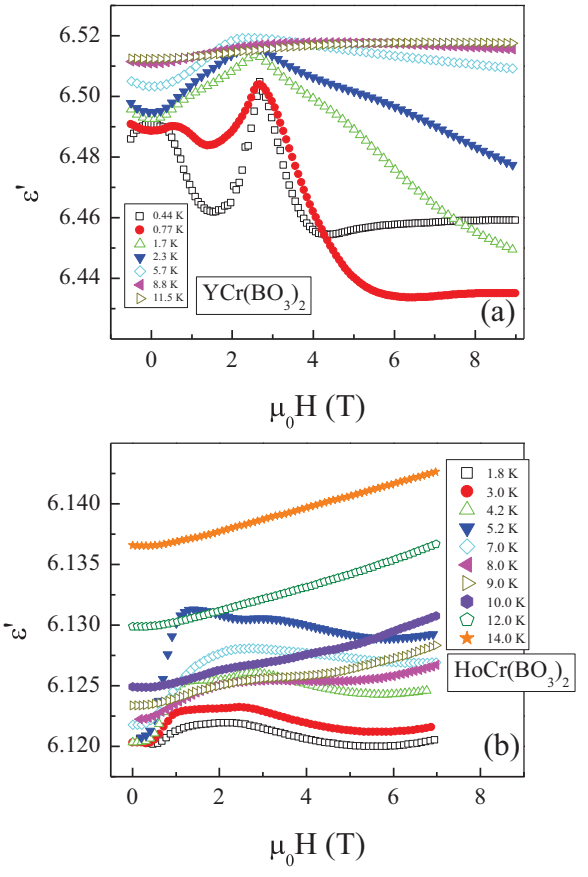

FIG. 11. The field dependence of the dielectric constant measured at 20 kHz at varying temperatures for (a) $YCr(BO_3)_2$ and (b) $HoCr(BO_3)_2$.

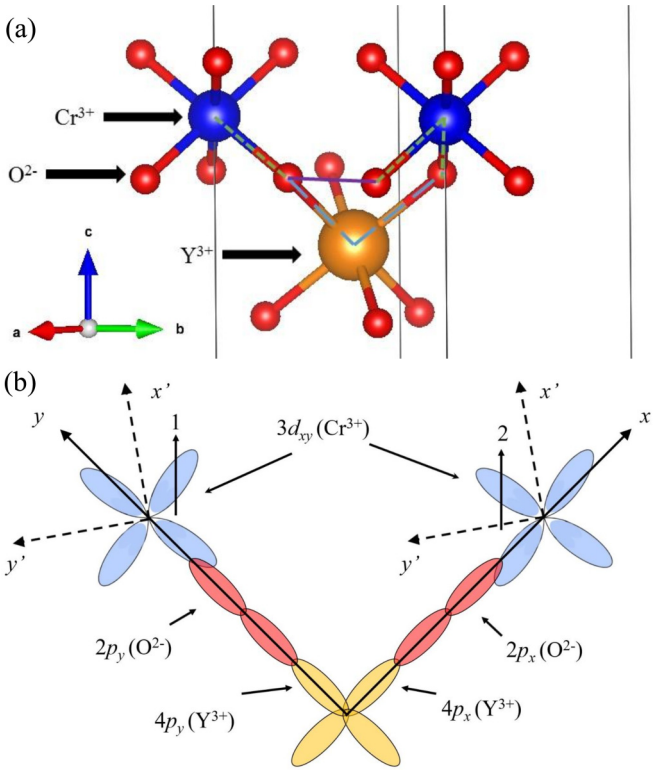

FIG. 12. (a) The lattice view of the Cr^{3+}-O^{2-}-O^{2-}-Cr^{3+} and the Cr^{3+}-O^{2-}-Y^{3+}-O^{2-}-Cr^{3+} superexchange paths, and (b) the orbital configurations related to the Cr^{3+}-O^{2-}-Y^{3+}-O^{2-}-Cr^{3+} superexchange path. The Cr^{3+} ions' frame of reference is denoted with primes. The angle between the unprimed and primed axes is 55°.

a canted AFM state below $T_N \approx 9$ K at zero field. With applied field above a critical vale of $H_C \approx 2.0$–2.5 T, the antiferromagnetic arrangement of the Cr^{3+} spins along the c axis is flipped to become ferromagnetic for both samples. The major difference here is that for the Ho compound, both the Ho^{3+} and the Cr^{3+} spins order ferromagnetically when $H > H_C$. This canted AFM state at zero field with spins aligning ferromagnetically in the ab plane and antiferromagnetically along the c axis of $YCr(BO_3)_2$ is consistent with the fact that its intralayer interaction is ferromagnetic and interlayer interaction is antiferromagnetic, which was revealed by the spin-wave spectrum simulation.

To understand why the intralayer interaction of the Y compound is ferromagnetic, we look into the superexchange interactions involving the Cr^{3+} ions. In order to qualitatively discuss the sign (FM or AFM) of the superexchange interactions, we turn to Kanamori theory. For a magnetic cation on an octahedral site, Kanamori has shown that the superexchange interaction via nonmagnetic anion is closely connected with the orbital states of the cation and anion [61]. In $YCr(BO_3)_2$, two superexchange pathways for the Cr^{3+} spins in the same layer are available as the CrO_6 octahedrons are connected by YO_6 octahedrons with corner-sharing oxygens. As shown in Fig. 12(a), the first is Cr^{3+}-O^{2-}-O^{2-}-Cr^{3+} and the second is Cr^{3+}-O^{2-}-Y^{3+}-O^{2-}-Cr^{3+}. As observed from other magnetic oxides, the Cr^{3+}-O^{2-}-O^{2-}-Cr^{3+} pathway's superexchange interaction is often AFM. Meanwhile, one possible situation for the Cr^{3+}-O^{2-}-Y^{3+}-O^{2-}-Cr^{3+} exchange path is shown in Fig. 12(b).

Here we consider the superexchange interaction between the spins on the d_{xy} orbitals of the Cr^{3+} ions. In the Cr^{3+} ions' frame of reference, the d_{xy} orbitals are centered 45° from both the x axis and the y axis. Through our Rietveld refinements of the neutron diffraction pattern, we determined that the Cr^{3+}-O^{2-}-Y^{3+} bond angle is 123.67(9)° and the O^{2-}-Y^{3+}-O^{2-} bond angle is 88.79(9)°, very close to 90°; therefore, the d_{xy} orbitals are centered ∼10° from the line where the O^{2-} and the Y^{3+} ions are situated, which allows for the necessary hybridization to occur between the d_{xy} and the p_x and p_y orbitals. In this configuration, the spin 1 on the left Cr^{3+} ion is transferred to the molecular orbital composed of the p_y orbitals of the O^{2-} $2p$ orbitals and the Y^{3+} $4p$ orbitals (the filled outermost orbitals), and the spin 2 on the right Cr^{3+} ion is transferred to the molecular orbital composed of the p_x orbitals of the O^{2-} and Y^{3+} ions. Due to Hund's rules, these two spins on the p_y and p_x orbitals in the Y^{3+} ions have to be parallel. Then, after these two spins are transferred back to the Cr^{3+} ion, a FM superexchange interaction is built. For $YCr(BO_3)_2$, it is reasonable to assume that this FM interaction overcomes the AFM interaction, leading to the FM spin arrangements in the ab plane.

In several other TLAF systems with layered perovskite structures, similar FM superexchange interactions involving $3d$-$2p$-$4p$ (or $3p$)-$2p$-$3d$ paths have been reported. For example, in $Ba_3CoNb_2O_9$ [62], a weak AFM interaction is the result of the FM Co^{2+}-O^{2-}-Nb^{5+}-O^{2-}-Co^{2+} superexchange interaction involving the Nb^{5+} $4p$ orbitals competing with the AFM Co^{2+}-O^{2-}-O^{2-}-Co^{2+} interaction. Accordingly, this system exhibits a small saturation field and a low AFM transition temperature. In another triangular lattice magnet, $AAg_2M(VO_4)_2$ (A=Ba, Sr; M=Co, Ni) [63], the FM Co^{2+}-O^{2-}-V^{5+}-O^{2-}-Co^{2+} interaction involving the V^{5+} $3p$ orbitals is stronger than the AFM Co^{2+}-O^{2-}-O^{2-}-Co^{2+} interaction resulting in a FM transition. One important note here for $YCr(BO_3)_2$ is that although the FM interaction overcomes the AFM interaction in the ab plane, the AFM interlayer interaction still leads to an AFM arrangement of spins along the c axis to stabilize the canted AFM spin structure. This interlayer interaction is weaker, but it plays an important role in defining the magnetic ground state.

Both $YCr(BO_3)_2$ and $HoCr(BO_3)_2$ show some MD behaviors. The Y compound's dielectric constant shows a slope change around T_N and a sharp peak around H_C; on the other hand, the Ho compound's dielectric constant shows a strong peak around T_N with an applied field and a broad peak around H_C. Apparently, this difference is related to the presence of the second magnetic ion, Ho^{3+}, in $HoCr(BO_3)_2$. To explain the MD anomalies, we first examined a possible linear magnetoelectric effect. For our system, both possible magnetic space groups, $R_I\bar{3}$ and $P_S\bar{1}$, contain an inversion center as one of their symmetry elements. Additionally, symmetry operators in both magnetic space groups do not break time-reversal symmetry. Therefore, the linear ME effect is excluded by symmetry.

We also observed that the cusp shape of the Y compound's MD anomaly is similar to behavior observed in the AFM $EuTiO_3$ [64,65]. In $EuTiO_3$, the pair correlation of the Eu

spins to a soft-phonon mode containing Eu-O stretching motions was ascribed to the MD anomaly. Such spin-phonon coupling was also attributed to the MD anomaly observed in a ferrimagnetic spinel Mn_3O_4 [66]. On the other hand, it is also possible that the higher-order, symmetry-independent ME terms can be relevant, as in the case for $TeCuO_3$ [67] and in Cr [$(H_3N\text{-}(CH_2)_2\text{-}PO_3(Cl)(H_2O)$] [68,69].

Another way to understand the differences between the MD effect in both samples is to consider magnetostriction. As the order of magnitude of the effect is fairly large ($\sim 10^{-3}$), we speculate that the differences in the dielectric constant data are more likely due to the magnetostriction caused by the extra exchange interaction between the Cr^{3+} and Ho^{3+} layers with an applied field rather than due to the change of the lattice parameters, which typically produces a much smaller anomaly ($10^{-5} \sim 10^{-6}$). Specifically, (i) at zero field, there is no exchange interaction between the Cr^{3+} and Ho^{3+} spins in $HoCr(BO_3)_2$ since only the Cr^{3+} spins order; therefore, there is no obvious dielectric anomaly around T_N. (ii) With an applied field $H < H_C$, the short-range ordering of Ho^{3+} spins could be induced, which can lead to an AFM exchange interaction between the Cr^{3+} and Ho^{3+} layers and result in magnetostriction. Thus, a small magnetic field such as 0.25 T induces a dielectric constant peak at around T_N. Moreover, with increasing field this effect is strengthened by involving more short-range ordered Ho^{3+} spins, and, consequently, the dielectric constant peak intensity increases. (iii) With even larger applied fields $H > H_C$, the Ho^{3+} spins order ferromagnetically along with the Cr^{3+} spins. This new spin structure possibly leads to weak magnetostriction compared to that of $H < H_C$. Therefore, the dielectric constant peak intensity achieves the highest value with $H = 1.0$ T and then decreases with increasing field as soon as it exceeds H_C, such as 3.0 T.

In any case, more studies are needed to determine the origin of the observed MD anomaly in both compounds. Experimental probes such as infrared and Raman spectroscopy could reveal possible spin-phonon coupling. Furthermore, dielectric constant and polarization (pyroelectric current) measurements on single-crystal samples can be helpful, not only to identify the ME coefficients for both compounds but also to study the possible magnetostriction effect for the Ho compound.

V. CONCLUSION

In summary, we report detailed experimental studies of the layered perovskites $RCr(BO_3)_2$ (R = Y and Ho) with triangular lattices, focusing on their magnetic and electric properties. We observed the presence of a canted AFM state in both samples at zero field for the Cr^{3+} spins as well as a FM state while a critical field was applied. More interestingly, in comparison to the Y compound, far different MD behaviors were observed in the Ho compound, which should be due to the interplay between the Cr and Ho magnetic layers. Our studies here demonstrate that the combination of layered structures with two different magnetic ions and triangular lattices can produce intriguing physical properties. This principle of materials engineering can help us to design and explore more complex magnetic materials.

ACKNOWLEDGMENTS

R.S. and H.D.Z. are thankful for support from the NSF-DMR through Award No. DMR-1350002. R.S. and H.D.Z. would also like to thank Dr. Stephen Nagler at ORNL for many enlightening conversations regarding this system. This research used resources at the High Flux Isotope Reactor, a DOE Office of Science User Facility operated by the Oak Ridge National Laboratory. A portion of this work was performed at the NHMFL, which is supported by National Science Foundation Cooperative Agreement No. DMR-1157490 and the State of Florida. E.S.C. and M.L. acknowledge support from the NSF-DMR-1309146.

[1] A. P. Ramirez, Annu. Rev. Mater. Sci. **24**, 453 (1994).
[2] M. F. Collins and O. A. Petrenko, Can. J. Phys. **75**, 605 (1997).
[3] L. Balents, Nature (London) **464**, 199 (2010).
[4] P.-W. Anderson, Mater. Res. Bull. **8**, 153 (1973).
[5] Y. Shimizu, K. Miyagawa, K. Kanoda, M. Maesato, and G. Saito, Phys. Rev. Lett. **91**, 107001 (2003).
[6] T. Itou, A. Oyamada, S. Maegawa, M. Tamura, and R. Kato, Phys. Rev. B **77**, 104413 (2008).
[7] P. Khuntia, R. Kumar, A. V. Mahajan, M. Baenitz, and Y. Furukawa, Phys. Rev. B **93**, 140408(R) (2016).
[8] Y. Zhou, K. Kanoda, and T.-K. Ng, Rev. Mod. Phys. **89**, 025003 (2017).
[9] Y. Li, D. Adroja, P. K. Biswas, P. J. Baker, Q. Zhang, J. Liu, A. A. Tsirlin, P. Gegenwart, and Q. Zhang, Phys. Rev. Lett. **117**, 097201 (2016).
[10] J. A. M. Paddison, M. Daum, Z. L. Dun, G. Ehlers, Y. Liu, M. B. Stone, H. D. Zhou, and M. Mourigal, Nat. Phys. **13**, 117 (2017).
[11] J. G. Cheng, G. Li, L. Balicas, J. S. Zhou, J. B. Goodenough, C. K. Xu, and H. D. Zhou, Phys. Rev. Lett. **107**, 197204 (2011).
[12] J. A. Quilliam, F. Bert, A. Manseau, C. Darie, C. Guillot-Deudon, C. Payen, C. Baines, A. Amato, and P. Mendels, Phys. Rev. B **93**, 214432 (2016).
[13] S. Nakatsuji, Y. Nambu, H. Tonomura, O. Sakai, S. Jonas, C. Broholm, H. Tsunetsugu, Y. Qiu, and Y. Maeno, Science **309**, 1697 (2005).
[14] A. Honecker, D. C. Cabra, H.-U. Everts, P. Pujol, and F. Stauffer, Phys. Rev. B **84**, 224410 (2011).
[15] P. Hauke, Phys. Rev. B **87**, 014415 (2013).
[16] T. Yoshida and C. Hotta, Phys. Rev. B **90**, 245115 (2014).
[17] S. Rachel, M. Laubach, J. Reuther, and R. Thomale, Phys. Rev. Lett. **114**, 167201 (2015).
[18] C. Stock, S. Jonas, C. Broholm, S. Nakatsuji, Y. Nambu, K. Onuma, Y. Maeno, and J.-H. Chung, Phys. Rev. Lett. **105**, 037402 (2010).
[19] S. Zhao, P. Dalmas de Réotier, A. Yaouanc, D. E. MacLaughlin, J. M. Mackie, O. O. Bernal, Y. Nambu, T. Higo, and S. Nakatsuji, Phys. Rev. B **86**, 064435 (2012).

[20] A. Yaouanc, P. Dalmas de Réotier, Y. Chapuis, C. Marin, G. Lapertot, A. Cervellino, and A. Amato, Phys. Rev. B **77**, 092403 (2008).

[21] T. Ono, H. Tanaka, H. Aruga Katori, F. Ishikawa, H. Mitamura, and T. Goto, Phys. Rev. B **67**, 104431 (2003).

[22] K. Kimura, H. Nakamura, K. Ohgushi, and T. Kimura, Phys. Rev. B **78**, 140401(R) (2008).

[23] L. F. Tocchio, H. Feldner, F. Becca, R. Valentí, and C. Gros, Phys. Rev. B **87**, 035143 (2013).

[24] H. Takatsu, G. Nénert, H. Kadowaki, H. Yoshizawa, M. Enderle, S. Yonezawa, Y. Maeno, J. Kim, N. Tsuji, M. Takata, Y. Zhao, M. Green, and C. Broholm, Phys. Rev. B **89**, 104408 (2014).

[25] C. Luo, T. Datta, Z. Huang, and D.-X. Yao, Phys. Rev. B **92**, 035109 (2015).

[26] Y. Shirata, H. Tanaka, A. Matsuo, and K. Kindo, Phys. Rev. Lett. **108**, 057205 (2012).

[27] H. D. Zhou, C. Xu, A. M. Hallas, H. J. Silverstein, C. R. Wiebe, I. Umegaki, J. Q. Yan, T. P. Murphy, J.-H. Park, Y. Qiu, J. R. D. Copley, J. S. Gardner, and Y. Takano, Phys. Rev. Lett. **109**, 267206 (2012).

[28] J. Ma, Y. Kamiya, Tao Hong, H. B. Cao, G. Ehlers, W. Tian, C. D. Batista, Z. L. Dun, H. D. Zhou, and M. Matsuda, Phys. Rev. Lett. **116**, 087201 (2016).

[29] N. Ikeda, K. Kohn, N. Myouga, E. Takahashi, H. Kitô, and S. Takekawa, J. Phys. Soc. Jpn. **69**, 1526 (2000).

[30] N. Ikeda, H. Ohsumi, K. Ohwada, K. Ishii, T. Inami, K. Kakurai, Y. Murakami, K. Yoshii, S. Mori, Y. Horibe, and H. Kito, Nature (London) **436**, 1136 (2005).

[31] T. Elkhouni, M. Amami, C. V. Colin, and A. Ben Salah, Mater. Res. Bull. **53**, 151 (2014).

[32] M. Lee, E. S. Choi, J. Ma, R. Sinclair, C. R. Dela Cruz, and H. D. Zhou, J. Phys.: Condens. Matter **28**, 476004 (2016).

[33] J. L. Robeiro, J. M. Perez-Mato, and L. G. Vieira, J. Magn. Magn. Mater. **416**, 15 (2016).

[34] S. Seki, Y. Onose, and Y. Tokura, Phys. Rev. Lett. **101**, 067204 (2008).

[35] Yu. A. Sakhratov, L. E. Svistov, P. L. Kuhns, H. D. Zhou, and A. P. Reyes, Phys. Rev. B **94**, 094410 (2016).

[36] T. Inami, Y. Ajiro, and T. Goto, J. Phys. Soc. Jpn. **65**, 2374 (1996).

[37] L. A. Prozorova, L. E. Svistov, A. I. Smirnov, O. A. Petrenko, L. N. Demianets, and A. Ya. Shapiro, J. Magn. Magn. Mater. **258-259**, 394 (2003).

[38] L. E. Svistov, A. I. Smirnov, L. A. Prozorova, O. A. Petrenko, A. Micheler, N. Büttgen, A. Ya. Shapiro, and L. N. Demianets, Phys. Rev. B **74**, 024412 (2006).

[39] M. Kenzelmann, G. Lawes, A.-B. Harris, G. Gasparovic, C. Broholm, A.-P. Ramirez, G.-A. Jorge, M. Jaime, S. Park, Q. Huang, A.-Ya. Shapiro, and L.-A. Demianets, Phys. Rev. Lett. **98**, 267205 (2007).

[40] M. Lee, E. S. Choi, X. Huang, J. Ma, C. R. De la Cruz, M. Matsuda, W. Tian, Z. L. Dun, S. Dong, and H. D. Zhou, Phys. Rev. B **90**, 224402 (2014).

[41] J. Hwang, E.-S. Choi, F. Ye, C. R. De la Cruz, Y. Xin, H.-D. Zhou, and P. Schlottmann, Phys. Rev. Lett. **109**, 257205 (2012).

[42] M. Lee, J. Hwang, E. S. Choi, J. Ma, C. R. De la Cruz, M. Zhu, X. Ke, Z. L. Dun, and H. D. Zhou, Phys. Rev. B **89**, 104420 (2014).

[43] D. I. Khomskii, J. Magn. Magn. Mater. **306**, 1 (2006).

[44] W. Eerenstein, N. D. Mathur, and J. F. Scott, Nature (London) **442**, 759 (2006).

[45] S.-W. Cheong and M. Mostovoy, Nat. Mater. **6**, 13 (2007).

[46] J. Hwang, E. S. Choi, H. D. Zhou, Y. Xin, J. Lu, and P. Schlottmann, Phys. Rev. B **85**, 224429 (2012).

[47] S. Oyama, M. Wakeshima, Y. Hinatsu, and K. Ohoyama, J. Phys.: Condens. Matter **16**, 1823 (2004).

[48] J. Hwang, E. S. Choi, H. D. Zhou, J. Lu, and P. Schlottmann, Phys. Rev. B **85**, 024415 (2012).

[49] M. Greenblatt, R. M. Hornreich, and B. Sharon, J. Solid State Chem. **10**, 371 (1974).

[50] J. Saha, G. Sharma, and S. Patnaik, J. Magn. Magn. Mater. **360**, 34 (2014).

[51] Y. Tokunaga, S. Iguchi, T. Arima, and Y. Tokura, Phys. Rev. Lett. **101**, 097205 (2008).

[52] Y. Doi, T. Satou, and Y. Hinatsu, J. Solid State Chem. **206**, 151 (2013).

[53] Z. L. Dun, X. Li, R. S. Freitas, E. Arrighi, C. R. De la Cruz, M. Lee, E. S. Choi, H. B. Cao, H. J. Silverstein, C. R. Wiebe, J. G. Cheng, and H. D. Zhou, Phys. Rev. B **92**, 140407(R) (2015).

[54] J. Rodriguez-Carvajal, Phys. B (Amsterdam, Neth.) **192**, 55 (1993).

[55] A. S. Wills, Phys. B (Amsterdam, Neth.) **276-278**, 680 (2000).

[56] M. I. Aroyo, J. M. Perez-Mato, D. Orobengoa, E. Tasci, G. de la Flor, and A. Kirov, Bulg. Chem. Commun. **43**, 183 (2011).

[57] M. I. Aroyo, J. M. Perez-Mato, C. Capillas, E. Kroumova, S. Ivantchev, G. Madariaga, A. Kirov, and H. Wondratschek, Z. Kristallogr. **221**, 15 (2006).

[58] M. I. Aroyo, A. Kirov, C. Capillas, J. M. Perez-Mato, and H. Wondratschek, Acta Crystallogr., Sect. A: Found. Crystallogr. **A62**, 115 (2006).

[59] J. M. Perez-Mato, S. V. Gallego, E. S. Tasci, L. Elcoro, G. de la Flor, and M. I. Aroyo, Annu. Rev. Mater. Res. **45**, 217 (2015).

[60] S. Toth and B. Lake, J. Phys.: Condens. Matter **27**, 166002 (2015).

[61] J. Kanamori, J. Phys. Chem. Solids **10**, 87 (1959).

[62] K. Yokota, N. Kurita, and H. Tanaka, Phys. Rev. B **90**, 014403 (2014).

[63] A. Möller, N. E. Amuneke, P. Daniel, B. Lorenz, C. R. Dela Cruz, M. Gooch, and P. C. W. Chu, Phys. Rev. B **85**, 214422 (2012).

[64] T. Katsufuji and H. Takagi, Phys. Rev. B **64**, 054415 (2001).

[65] V. V. Shvartsman, P. Borisov, W. Kleemann, S. Kamba, and T. Katsufuji, Phys. Rev. B **81**, 064426 (2010).

[66] R. Tackett, G. Lawes, B. C. Melot, M. Grossman, E. S. Toberer, and R. Seshadri, Phys. Rev. B **76**, 024409 (2007).

[67] G. Lawes, T. Kimura, C. M. Varma, M. A. Subramanian, N. Rogado, R. J. Cava, and A. P. Ramirez, Prog. Solid State Chem. **37**, 40 (2009).

[68] G. Nénert, U. Adem, E. M. Bauer, C. Bellitto, G. Righini, and T. T. M. Palstra, Phys. Rev. B **78**, 054443 (2008).

[69] G. Nénert, H.-J. Koo, C. V. Colin, E. M. Bauer, C. Bellitto, C. Ritter, G. Righini, and M.-H. Whangbo, Inorg. Chem. (Washington, DC) **52**, 753 (2013).